Monthly Notices of the ROYAL ASTRONOMICAL SOCIETY

MNRAS **522,** 3753–3765 (2023)
Advance Access publication 2023 April 13

https://doi.org/10.1093/mnras/stad1076

Cold molecular gas outflow encasing the ionized one in the Seyfert galaxy NGC 3281

Bruno Dall'Agnol de Oliveira [1]★ Thaisa Storchi-Bergmann,[1] Raffaella Morganti [2,3] Rogemar A. Riffel [4] and Venkatessh Ramakrishnan[5,6]

[1]*Departamento de Astronomia, Universidade Federal do Rio Grande do Sul, IF, CP 15051, 91501-970 Porto Alegre, RS, Brazil*
[2]*ASTRON, the Netherlands Institute for Radio Astronomy, Oude Hoogeveensedijk 4, NL-7991 PD Dwingeloo, the Netherlands*
[3]*Kapteyn Astronomical Institute, University of Groningen, Postbus 800, NL-9700 AV Groningen, the Netherlands*
[4]*Departamento de Física, CCNE, Universidade Federal de Santa Maria, 97105-900, Santa Maria, RS, Brazil*
[5]*Finnish Centre for Astronomy with ESO, University of Turku, FI-20014 Turku, Finland*
[6]*Astronomy Department, Universidad de Concepción, Barrio Universitario S/N, Concepción 4030000, Chile*

Accepted 2023 April 6. Received 2023 April 5; in original form 2023 February 23

ABSTRACT

We present ALMA CO (2-1) observations of the Seyfert 2 galaxy NGC 3281 at ∼100 pc spatial resolution. This galaxy was previously known to present a bi-conical ionized gas outflow extending to 2 kpc from the nucleus. The analysis of the CO moment and channel maps, as well as kinematic modelling, reveals two main components in the molecular gas: one rotating in the galaxy plane and another outflowing and extending up to ∼1.8–2.6 kpc from the nucleus, partially encasing the ionized component. The mass of the outflowing molecular gas component is $M_{\rm mol,\,out} = (2.5 \pm 1.6) \times 10^6\,{\rm M}_\odot$, representing ∼1.7–2 per cent of the total molecular gas seen in emission within the inner 2.3 kpc. The corresponding mass outflow rate and power are $\dot{M}_{\rm out,mol} = 0.12$–$0.72\,{\rm M}_\odot\,{\rm yr}^{-1}$ and $\dot{E}_{\rm out,mol} = (0.045$–$1.6) \times 10^{40}$ erg s^{-1} , which translates to a kinetic coupling efficiency with the AGN power of only 10^{-4}–0.02 per cent. This value reaches up to 0.1 per cent when including both the feedback in the ionized and molecular gas, as well as considering that only part of the energy couples kinetically with the gas. Some of the non-rotating CO emission can also be attributed to inflow in the galaxy plane towards the nucleus. The similarity of the CO outflow – encasing the ionized gas one and the X-ray emission – to those seen in other sources, suggests that this may be a common property of galactic outflows.

Key words: molecular data – galaxies: active – ISM: jets and outflows – galaxies: individual (NGC 3281) – galaxies: Seyfert.

1 INTRODUCTION

The energy released by active galactic nuclei (AGNs), as a consequence of accretion of matter to a nuclear supermassive black hole (SMBH), couples at different degrees with the interstellar and intergalactic mediums. This feedback process has been claimed to play an important role in the evolution of the galaxies (e.g. Fabian 2012; Silk & Mamon 2012) by decreasing the galaxy star formation rate (SFR; negative feedback; e.g. Cano-Díaz et al. 2012; Cicone et al. 2014) or even raising it (positive feedback; e.g. Maiolino et al. 2017; Gallagher et al. 2019).

None the less, direct evidence of an impact at large scales – reaching beyond the galaxy limits – has been mostly observed in massive elliptical galaxies, impacting their surrounding hot haloes, via mechanical energy released by a nuclear radio jet preventing or slowing the halo cooling rate (e.g. Cavagnolo et al. 2010; Fabian 2012). The related feedback mechanism has been referred to as radio/jet/mechanical mode and is characterized by a low-mass accretion rate to the SMBH, with Eddington ratio $\lambda_{\rm Edd} \lesssim 1$ per cent (Heckman & Best 2014).

AGN feedback may also be dominated by another mechanism – the radiative/quasar-mode feedback – in which the energy is primarily released through radiation and winds from the accretion disc (Morganti 2017), and the mass accretion to the SMBH occurs at a high rate, with $\lambda_{\rm Edd} \gtrsim 1$ per cent (Heckman & Best 2014). However, the radiative-mode feedback has sparse evidences of an impact at large – galactic to extragalactic scales (Fabian 2012).

The energy released by the AGN can interact with the gas at different phases (Harrison et al. 2018), with the ionized phase being the most studied. However, in previous observations of outflows of ionized gas, the fraction of the AGN bolometric luminosity ($L_{\rm AGN}$) that couples kinematically with the ionized gas is usually not large enough to affect the evolution of the galaxies (e.g. Husemann et al. 2016; Spence et al. 2018; Dall'Agnol de Oliveira et al. 2021), with typical values below 0.5–5 per cent, the minimum required by some models (e.g. Di Matteo, Springel & Hernquist 2005; Hopkins & Elvis 2010; Zubovas 2018) and used in the feedback recipes of cosmological simulations (e.g. Schaye et al. 2015; Nelson et al. 2019). But one might be cautious when comparing observations with models/simulations (Harrison et al. 2018), since the percent of the total outflow energy that is kinetic can be little as ∼20–30 per cent (Richings & Faucher-Giguère 2018).

★ E-mail: bruno.ddeo@gmail.com

It is also important to consider the energy feedback other gas phases, such as the neutral atomic, the molecular and the highly ionized gas (Cicone et al. 2018). Of great importance is the molecular gas phase, specially at low temperatures ($T < 100$ K). Alongside with the neutral atomic gas phase, the cold molecular gas is the fuel to form new stars (Veilleux et al. 2020; Saintonge & Catinella 2022). Any large impact on these gas phases will therefore affect the growth of the host galaxies.

One way to look for a direct global impact of AGN feedback over the cold molecular gas is to compare its content on AGN host galaxies relative to control galaxy samples. Signs of gas depletion in AGN hosts may indicate that this component has been destroyed or removed from the galaxy disc. Measurements of the fraction ($f_{\rm H_2}$) of molecular gas mass ($M_{\rm mol}$) relative to the total stellar mass (M_*), measured for the host galaxies of local AGNs, shows similar values of $f_{\rm H_2}$ in comparison with control samples (e.g. Rosario et al. 2018; Jarvis et al. 2020; Salvestrini et al. 2022), although there are sparse evidence of depletion in high-z objects (e.g. Bischetti et al. 2019; Circosta et al. 2021). Equivalent results are found for the specific SFR $sSFR = SFR/M_*$ in AGN, for which it is observed a null or positive trend between the SFR and $L_{\rm AGN}$ (e.g. Ji et al. 2022; Kim et al. 2022), which may be interpreted as the AGN not affecting the efficiency at which new stars are born. None the less, Ward et al. (2022) did not find a relative decrease in the $f_{\rm H_2}$ and $sSFR$ of AGN in cosmological simulations, even though the inclusion of AGN feedback recipes are required to reproduce some observables such as the stellar mass function of galaxies (Naab & Ostriker 2017).

Since a global view of the molecular content shows ambiguous results, high spatial resolution observations may shed some light on the effect of the AGN feedback on the cold molecular gas, specially if compared with other gas phases such as the ionized one. For such, we can study local AGNs, since they can be observed with high-signal-to-noise ratio at such spatial resolutions, using radio interferometers in (sub)milimetre wavelengths such as the Atacama Large Millimetre/submillimetre Array.

In this work, we analyse the molecular gas content of the local Seyfert 2 spiral galaxy NGC 3281[1], with bulge-to-total luminosity ratio of B/T ~ 0.1 (Gao et al. 2019). It has a Compton-thick nucleus with a column density of $\sim 2 \times 10^{24}$cm^{-2} (Vignali & Comastri 2002; Sales et al. 2011), being part of the Swift Burst Alert Telescope catalog (Oh et al. 2018), and has been classified as a hidden/buried source (Winter et al. 2009). From the observed [O III] luminosity $L_{[O\,iii]} = 10^{40.74}$ erg s^{-1} (Schmitt et al. 2003), we obtain a bolometric luminosity of $L_{\rm Bol} = 10^{44.3 \pm 0.4}$ erg s^{-1} using the relations of Heckman et al. (2004). This value is compatible with the value from Vasudevan et al. (2010, for the high N_H case) and Stone et al. (2016), but lower than $10^{45.28}$ erg s^{-1} from Sales et al. (2011). Vasudevan et al. (2010) also provide an estimate for SMBH mass of $M_{BH} \sim 10^{7.2}$ M$_\odot$ from the K-band bulge magnitude. The literature present a wide range of values for the total stellar mass of NGC 3281, with values ranging between $10^{8.6}$ M$_\odot$ (Winter et al. 2009, as derived from the 2MASS K-band magnitude) and $10^{10.24}$ M$_\odot$ (Koss et al. 2011, from stellar population fit to the ugriz photometry), with a value of $10^{9.6}$ M$_\odot$ from Hess et al. (2015, as derived from its WISE colours).

We observed the CO (2-1) line – which is a tracer for the cold H_2 (Bolatto, Wolfire & Leroy 2013a) – in NGC 3283, using interferometry data from ALMA with a spatial resolution of $\sim$0.5 arcsec $\sim$ 100 pc. In Section 2, we describe the observations, alongside with ancillary data from other instruments. In Section 3, the methodology and results are presented, including the identification of molecular outflows and inflows of the CO line. In Section 4, we discuss the scenario of NGC 3281, comparing it with previous works. In this section, we also obtain the molecular mass outflow and its energetics. And finally, in Section 5, we summarize the conclusions. Throughout the paper, we use an angular scale of 0.23 kpc arcsec^{-1} corresponding to a luminosity distance D_L of 48.54 Mpc, obtained for a $H_0 = 70$ km s^{-1}, $\Omega_{\rm M} = 0.27$, and $\Omega_\Lambda = 0.7$ cosmology, using a redshift of z = 0.01124 (see Section 3.2.1). Unless otherwise specified, all velocities are in the Kinematic Local Standard of Rest (LSRK) and use a radio velocity definition.

2 OBSERVATIONS

2.1 ALMA data

NGC 3281 was observed with ALMA on 2019 April 17 in Cycle 6 (ID: 2018.1.00211.S, PI: Ramakrishnan, V.). Four spectral windows (SPW) were used, centred on the observed frequencies 228.084, 229.938, 215.389, and 217.070 GHz. The first one contains the desired emission line of CO (2-1) (230.538 GHz rest frequency), having 480 channels in a 1.875 GHz bandwidth, and a spectral resolution (channel width) of Δv = 5.14 km s^{-1}. The other three SPWs contain 128 channels with 2 GHz bandwidth and were used to detect the 217–233 GHz rest frequency continuum and remove the underlying continuum emission from the emission line.

We used the default Alma Pipeline Reduction, which resulted in a continuum-subtracted cube, that has a synthesized beam with full width at half-maximum of FWHM = 0.57 × 0.46 arcsec^2 and Position Angle of PA = -64.4°, and a pixel width (spatial dimension) of CDELT = 0.09 arcsce. The de-convolution and imaging used Briggs weighting with a robust parameter of 0.5. The RMS at the centre of the field is 0.79 mJy BEAM^{-1} over the channel width. This is the value prior to primary beam response correction. Throughout the paper, we used a rms 2D map, obtained by dividing the rms 1D value by the primary beam response image. This gives a more fiducial rms threshold value, being 1.5 times higher than the central value at 10 arcsec from the nucleus, and five times at the end border of the field.

2.2 Ancillary data

In Fig. 1, we show the BVI colour-composite image of the galaxy from Ho et al. (2011)[2], obtained with the du Pont telescope, which reveals that the galaxy has its plane inclined by $\sim 69^\circ$ relative to the plane of the sky and is warped in the outer regions, with a line of nodes at PA $\sim 138^\circ$ (Rubin et al. 1985; Storchi-Bergmann, Wilson & Baldwin 1992; Ho et al. 2011). The insert shows an optical continuum image obtained with the Hubble Space Telescope (hereafter *HST*) through the filter F606W, with darker regions tracing dust in the galaxy. The contours show the region where a narrow-band [O III]λ5007 image (in red), as well as a soft X-Rays 0.3–3 keV one (in blue, at (10^{-3}, $10^{-2.4}$, and $10^{-1.8}$) counts spaxel^{-1}), reveal a bipolar structure, to the North and South of the nucleus, attributed to an AGN-driven outflow (Storchi-Bergmann et al. 1992). As concluded by these authors, the NE is the far side of the galaxy and the SW is its near side, and thus, while the outflow to the North

[1] See also https://dc.zah.uni-heidelberg.de/sasmirala/q/prod/qp/NGC%203281 for a comprehensive summary (Asmus et al. 2014)

[2] https://cgs.obs.carnegiescience.edu/CGS/object_html_pages/NGC3281.html (Ho et al. 2011)

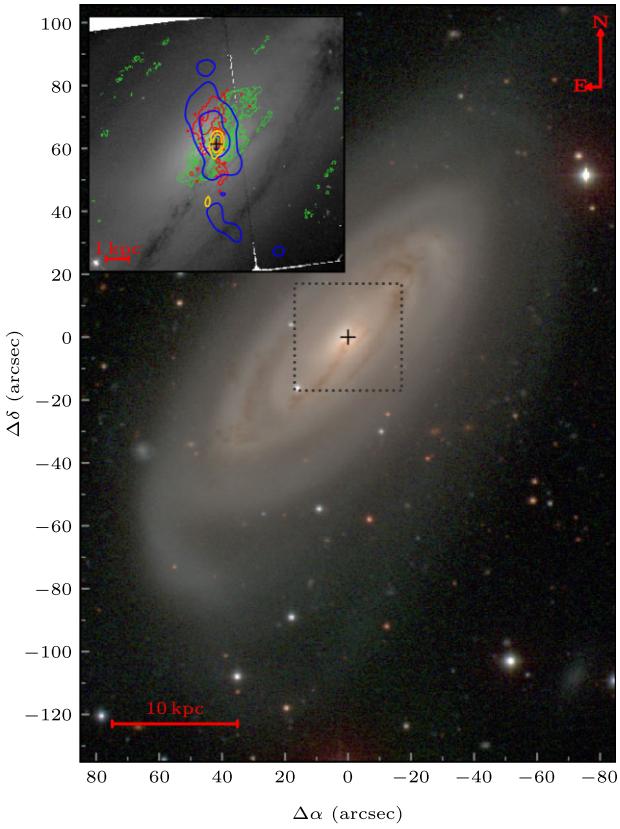

Figure 1. Global view of NGC 3281. The colour-composite image (from the du Pont telescope) shows the presence of spirals and dust. The zoomed-in region (delineated by the dotted box) shows the *HST* continuum image obtained through the F606W filter and includes the contours of the (*HST*) [O III] narrow-band image (red), the Chandra's soft X-Rays 0.3–3 keV image (blue; Ma et al. 2020), the *ATCA* radio 8.6 GHz image (yellow; Morganti et al. 1999), and the M_0 from CO (2-1; green, also shown in Fig. 2). The cross marks the position of the nucleus, defined as the peak of the 230 GHz continuum. The outer regions of the large-scale image shows that the stellar disc is warped at larger scales.

is projected against the far side of the galaxy, the southern part of the outflow is partially hidden by the near side of the galaxy plane. The yellow contours purple (at 5 and 20 $\times$ $\sigma_{\rm RMS\,=\,0.2\,mJy\,beam^{-1}}$) show that this galaxy has a somewhat compact radio emission at $\sim$1 arcsec spatial resolution (Morganti et al. 1999), showing a second blob of 3.5 cm (8.6 GHz) emission at $\sim$8 arcsec approximately to the South of the nucleus, at a Position Angle of $\sim$170°, with a signal-to-noise ratio of $\sim$9. Therefore, we cannot discard the presence of a radio jet, which has been claimed to have important role in the feedback even in radio-quiet objects in quasar-mode (Jarvis et al. 2019).

Fig. 1 also includes the flux distribution (moment M_0) of the CO (2-1) in emission as green contours (see Section 3.1) in order to show the location of the region corresponding to the CO emission – that is the main focus of the discussion in the next sections and figures – relative to the host galaxy.

Both *HST* images were retrieved from the Mikulski Archive for Space Telescopes. The F606W continuum image proposal ID is 8598 and the galaxy was observed on 1995 April 01, while the proposal ID for which the [O III] image was obtained is 5479 and the observations conducted on 2001 March 03 (Schmitt et al. 2003). The [O III] image was continuum-subtracted using an image observed as part of the same proposal. Both images have been cleaned from an excess of cosmic rays.

The soft X-ray data (events) was collected from the Chandra Data Archive and corresponds to observations made on 2019 January 24 with ObsID 21 419 (Ma et al. 2020). We performed the same reduction steps described by the authors to generate an adaptively smoothed image over the 0.3–3 keV spectral range.

The 8.6 GHz radio data were observed with the Australia Telescope Compact Array (*ATCA*) on 1995 July 19 (project code C405), and the reduction process are described in Morganti et al. (1999).

3 METHODOLOGY AND RESULTS

We have analysed the ALMA data using measurements of the moments and fitting a 3D model to the CO (2-1) emission line profiles with the ^{3D}BAROLO package (Di Teodoro & Fraternali 2015). We further analysed the data using channel maps of the CO (2-1).

3.1 Moments

In order to provide a global view of the distribution and kinematics of the cold molecular gas in NGC 3281, we have obtained moment maps M_0, M_1, and M_2 of CO, as described in Appendix A.

The CO moment maps of NGC 3281 are shown in the second row of Fig. 2, following the layout of a previous similar study of our group (Ramakrishnan et al. 2019). Only channels with flux densities above $3\sigma_{\rm RMS}$ were used. We performed the moments calculations in a cube re-binned by collapsing four channels into one (from channels with $\Delta v = 5.14$ km s^{-1} to channels with $\Delta v = 20.55$ km s^{-1}, in radio units at rest), which reduced the noise without affecting the resulting moments values. We note that M_2 values below $\sim$20 km s^{-1} are quite uncertain, since they originate mostly from spectra profiles, for which the moments were calculated using less than 5 spectral pixels (given the $3\sigma_{\rm RMS}$ threshold). Using the original non-binned cube improved the results in only few spectra, since these are the ones with lower signal-to-noise ratio values. M_0 and M_1 are less affected by this problem.

The upper-right panel of Fig. 2 shows the integrated spectrum in red (using only non-masked regions, see right-hand panel in Fig. B1), both for the cube with the original channel width (lighter colour) and the re-binned one (darker). In this case, we integrated spectra from the spaxels that were not emission dominated: the spaxels not masked in the CO moments maps. Only spaxels inside a 13 arcsec radius were considered in order to avoid spectra with lower signal to noise from the outer regions.

In the upper-left panel of Fig. 2, we added the M_0 green contours over the *HST* optical continuum image, alongside with the *HST* [O III] image red contours. The diagonal dashed black line marks the galaxy major axis (see Section 3.2.1), where we identified the far/near sides in the upper-left panel. As expected, there is more dust blocking the stellar continuum in the near side (black lanes, see also Fig. 1). We can also see that the flux distribution of the molecular gas in emission (green contours) is well correlated with the dust lanes, which is expected since the two are usually seen together in galaxies (e.g. Alves, Lada & Lada 1999), with the dust even been used as a tracer of molecular gas column density (Bolatto et al. 2013a). The dust also helps to protect the molecules from dissociation caused by the radiation field. In contrast, the ionized gas – as traced by the [O III] – is not correlated with CO and shows a bipolar cone-like structure not in the disc, but at an angle to it (also noted in Storchi-Bergmann et al. 1992). It is more visible to the North/North-East direction (above the galaxy disc), as its southern counterpart is partially hidden by the

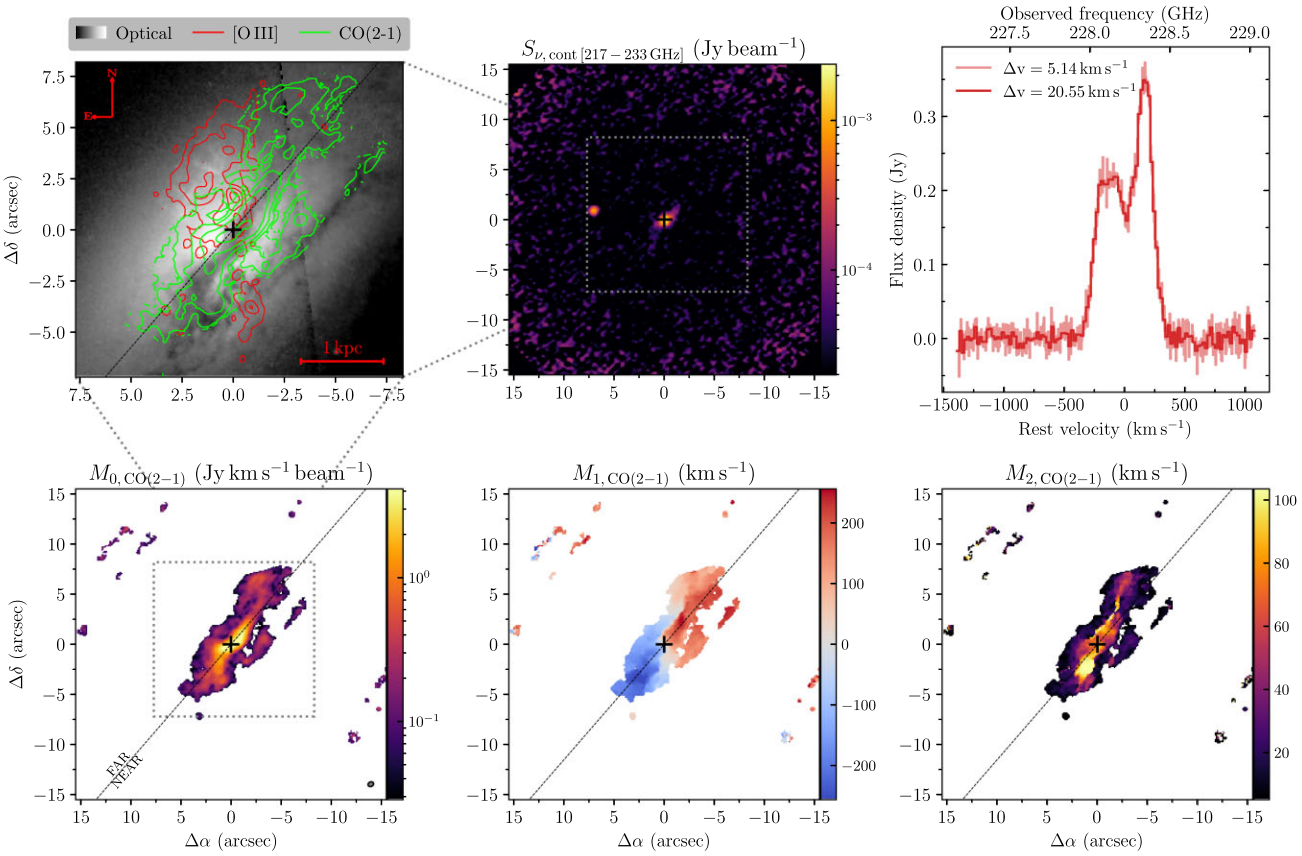

Figure 2. Optical images and CO measurements of NGC 3281. Upper left: HST optical F606W continuum image with superposed contours of [O III] (red) and CO (2-1) (green). This panel is a zoom-in of the remaining maps of this figure, as indicated by the grey dotted boxes. Upper centre: sub-millimetre continuum image. Upper right: CO-integrated spectra, obtained from spaxels used to obtain the moments of the CO in emission. The light colours correspond to a spectral resolution of $\Delta v = 5.14\,\mathrm{km\,s^{-1}}$, with the darker referring to the $\Delta v = 20.55,\mathrm{km\,s^{-1}}$ re-sampled cube. Lower left, centre, and right: the three moments of the CO in emission. The bottom-left panel shows the synthesized beam (grey ellipse in the bottom-right corner) and near/far sides of the galaxy disc plane.

near-side of the disc, as previously mentioned. The bipolar structure is also seen in soft-X-ray (Ma et al. 2020) also with the emission stronger at the far side (above the disc).

3.1.1 Sub-milimetre continuum and possible companions

The middle-upper panel of Fig. 2 corresponds to the continuum between 217 and 233 GHz rest frequency, generated from the channels used to subtract the continuum from the data cube. We see a nuclear emission (∼0.9 arcsec radius) with a very weak linear – or 'S' shape – emission (∼3 arcsec maximum radius extent), which follows the CO emission. There is also a second blob of emission (∼7 arcsec to the East, with a ∼0.7 arcsec radius). We do not find any counterpart in other wavelengths for this localized emission, and therefore, we cannot distinguish if the origin comes from an object close to NGC 3281, or far away from it along the line of sight. In the first case, it could be an object (e.g. a dwarf galaxy) that has recently passed close to the nuclear region. In this case, it could be related to the current event of nuclear accretion of gas, which may have 'turned on' the AGN.

We also note that, there is – at $[\Delta\alpha,\ \Delta\delta) \sim (60\,\mathrm{arcsec}, -35\,\mathrm{arcsec})$] in Fig. 1– a faint blob of emission in the optical, with ∼1.7 arcsec radius, coming from another object that could also be related to the AGN activity. If this is the case, the apparent dust trail that seems to connect the object with the nucleus – extending from the nucleus to the South-East, could be a trace of this interaction. In fact, NGC 3281 has been identified as part of the nearby Antlia cluster (e.g. Hess et al. 2015), with a projected distance ∼0.6° ∼ 0.5 Mpc from the cluster's centre (which we assumed to be in NGC 3268). Since NGC 3281 is in a somewhat denser environment, this may increase the chance of minor merger events, which could be the origin of the blob of emission in the optical.

Hess et al. (2015) also reports a H I detection without an optical counterpart, ∼0.1° ∼ 85 kpc to the East of NGC 3281, which may be debris from a previous galaxy interaction. Supporting this hypothesis, from the ∼200 sources with similar characteristics – H I emission without previous optical counterpart – Haynes et al. (2011) found that 3/4 are probably associated with tidal debris.

However, none of the above hypotheses can be verified with our current data.

3.2 Kinematics

3.2.1 Tilted-rings model

We model the global kinematics of the CO (2-1) using the software ^{3D}BAROLO (Di Teodoro & Fraternali 2015). In this model's approach, tilted-ring models are fitted over the entire data cube in the spectral region covered by the selected emission line, different from the

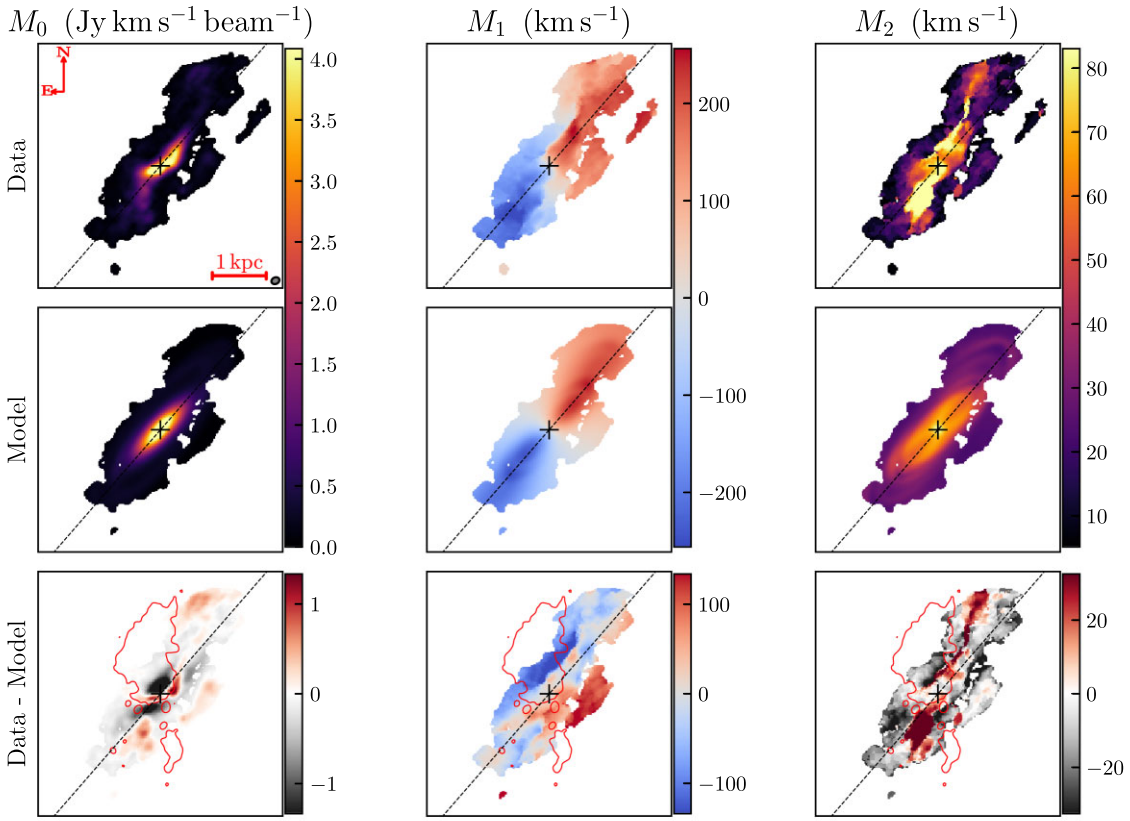

Figure 3. Fitting results of NGC 3281 kinematics using ^{3D}BAROLO. The first, second, and third columns show the three moments of the data (first row), the 3D model (second row), and the corresponding residuals (last row).

traditional 2D methods, that fit a disc model over a previously generated velocity field map (e.g. M_1).

With 3D models, it is possible to generate other moment maps (besides the velocity map M_1). In Fig. 3 (based on one of the ^{3D}BAROLO output figures), the three columns show, from left to bottom, the M_0, M_1, and M_2 maps of the original data cube (first row), the model (middle), and the residuals (last row). Fig. C1 shows the result of the fit of a 2D tilted-rings to the M_1 map (from Begeman 1987), modelled using the same software.

Initial parameters used in the modelling include the central position (taken from the sub-millimetre continuum), inclination $i = 69°$, and major axis position angle PA $= 140°$ (the code is sensitive to these last two-parameter guesses). We adopt the following quantities as free parameters: rotational velocity, velocity dispersion, i, and PA (the last two being allowed to vary by $\pm 5°$ along the radius).

We first ran the 3D fit leaving the systemic velocity as a free parameter, which resulted in the best-fitting value of $v_{sys} \sim 3332$ km s^{-1}, in the LSRK referential frame and for a relativistic velocity definition. Using the corresponding redshift ($z = 0.01124$), we set the data cube to the rest frame and re-fitted the data, using now a fixed $v_{sys} = 0$ km s^{-1}, and keeping the same initial PA and i values, cited above.

From the final best fit, we obtained a mean i and PA values of 139° and 73° (dashed black line in Fig. 2 and in the following ones), respectively. We note that by varying the initial values of i and PA by $\pm 10°$, fitting results with similar residuals are obtained, which do not affect our following analysis/conclusions below. With initial parameters outside this range, the residuals increase significantly.

Fig. 3 shows that the M_1 – and respective residuals – calculated from the 3D model (second row) and the one fitted in the 2D model (last row) are quite similar. This is expected, since, for high-resolution data (as is our case), 2D models return reliable fits to the line-of-sight field kinematics (Di Teodoro & Fraternali 2015). Given this equivalence, we use only the 3D model in this paper.

The M_1 map shows small residuals along the major axis (within a projected width of $\sim$1.8 arcsec $\sim$400 pc), but higher values perpendicular to it (up to ~ 100 km s^{-1}), in the direction of the [O III] emission (red contours in Fig. 3). The M_2 and M_0 maps also show high discrepancies. Noticeably, M_2 shows positive high-residuals along a strip (redder values in the residual map), which starts parallel to the major axis, but deviates to the North in the far side, and to the South in the near side. This 'line' separates the region where the bulk of molecular gas follows a more ordered rotational motion (along the major axis), and the perpendicular region containing the remaining molecular gas emission. There is also a significant deviation in the M_0 residuals close to the nuclear region.

3.2.2 *CO emission-line profiles*

In Fig. 4, we show a grid of CO (2-1) emission-line profiles overplotted on the first moment map to identify its location over the molecular gas distribution. Each spectrum corresponds to the sum of all spectra – that were not masked – inside cells with size equals to one mean FWHM. There is a clear complexity in the profiles, including multiple components.

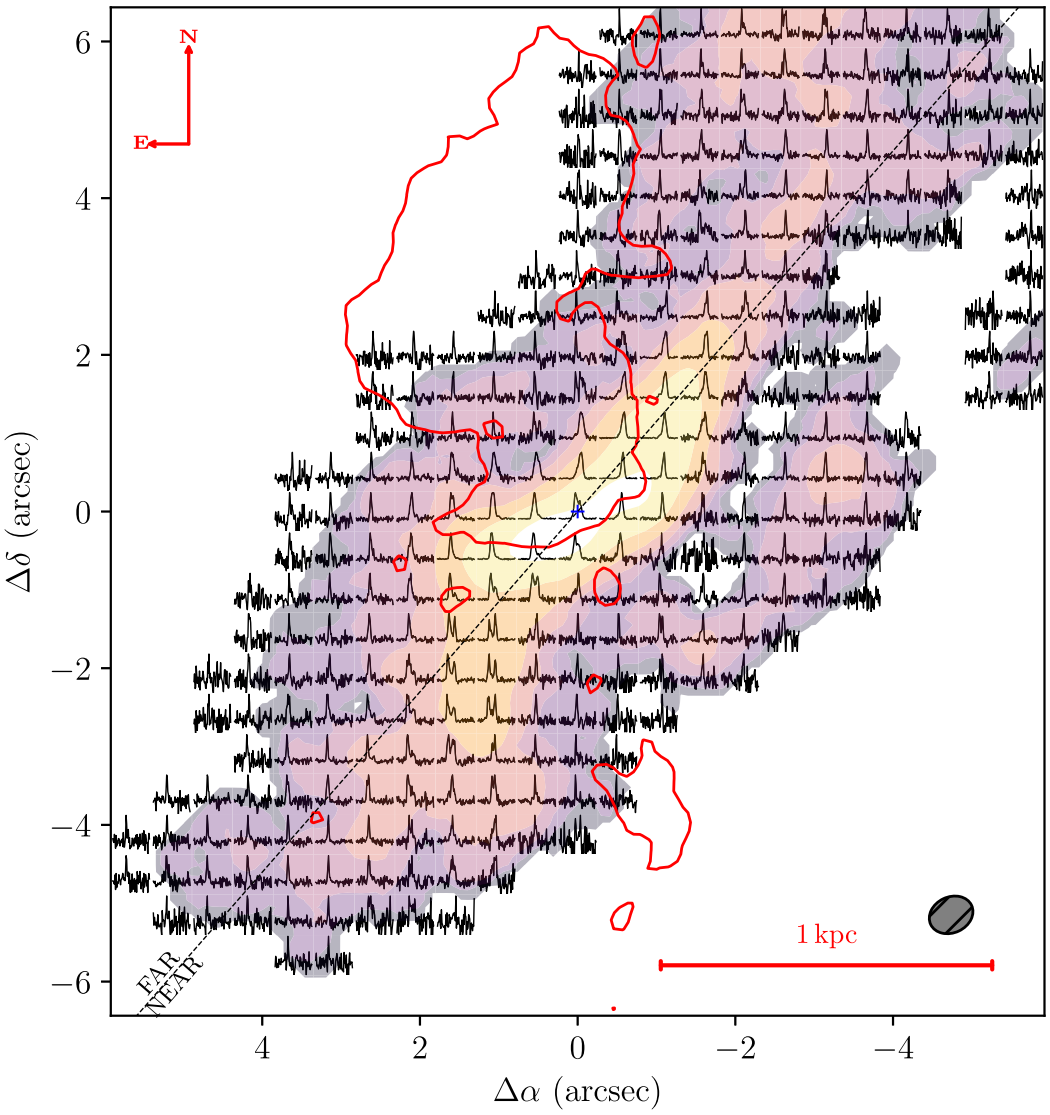

Figure 4. Grid of spectra from the NGC 3281 ALMA data cube, overploted over the M_0. Only spaxels with emission-dominated spectra were considered. The grid has cells with width/length equal to the mean value of the beam FWHM (grey ellipse in the bottom right). Each spectrum corresponds to the sum of all spectra inside each cell. The outer contour of [O III] emission is shown in red.

For example, the strip with high M_2 residuals (reddest values in the lower right panel of Fig 3) is located in a region with double-peaked profiles. In Appendix A (Fig. A1), we show that double-peaked profiles can present the same moments as single-peak ones, which reveals that there is a degeneracy in the moments values for different line profiles. Therefore, it is important to also look at the distribution of emission-line profiles over the observed field. Comparing the profiles distribution with the moment maps, we note that – along the major axis – there is a component that dominates the emission and is tracing molecular gas with circular motion in the galaxy plane. However, perpendicular to it, we see a prevalence of emission line profiles with components that capture peculiar – non-rotational motions – in the molecular gas. The strip with high M_2 residuals therefore shows the intersection of these two kinematically different regions, where the components have similar intensities. This also seems to be the origin of the S-shape morphology seen in the M_0 map, since it includes the sum of the fluxes from both components.

3.2.3 *Channel maps*

We have also obtained channel maps from the data, comparing them with the ^{3D}BAROLO model in Fig. 5. Each panel shows the integrated flux within channels with width $\Delta v = 41\,km\,s^{-1}$ velocity width, cutting values below the corresponding σ_{RMS}. Superposed in each map are the contours of the 3D model (in white) and the [O III] line emission (red).

Once again, the channel maps show that the 3D model can reproduce the data of the CO along the kinematic major axis (white dotted line). However, even along the region dominated by rotation, the fit is far from perfect, with the highest deviations seen in the channels with highest absolute velocities: above $171\,km\,s^{-1}$ and below $-281\,km\,s^{-1}$. None the less, the fit is useful to identify regions that clearly deviate from disc rotation kinematics. We identify in the channel maps of Fig. 5 four such regions, A_1, A_2, B_1, and B_2, which are highlighted as green and blue ellipses in Fig. 5, as described below.

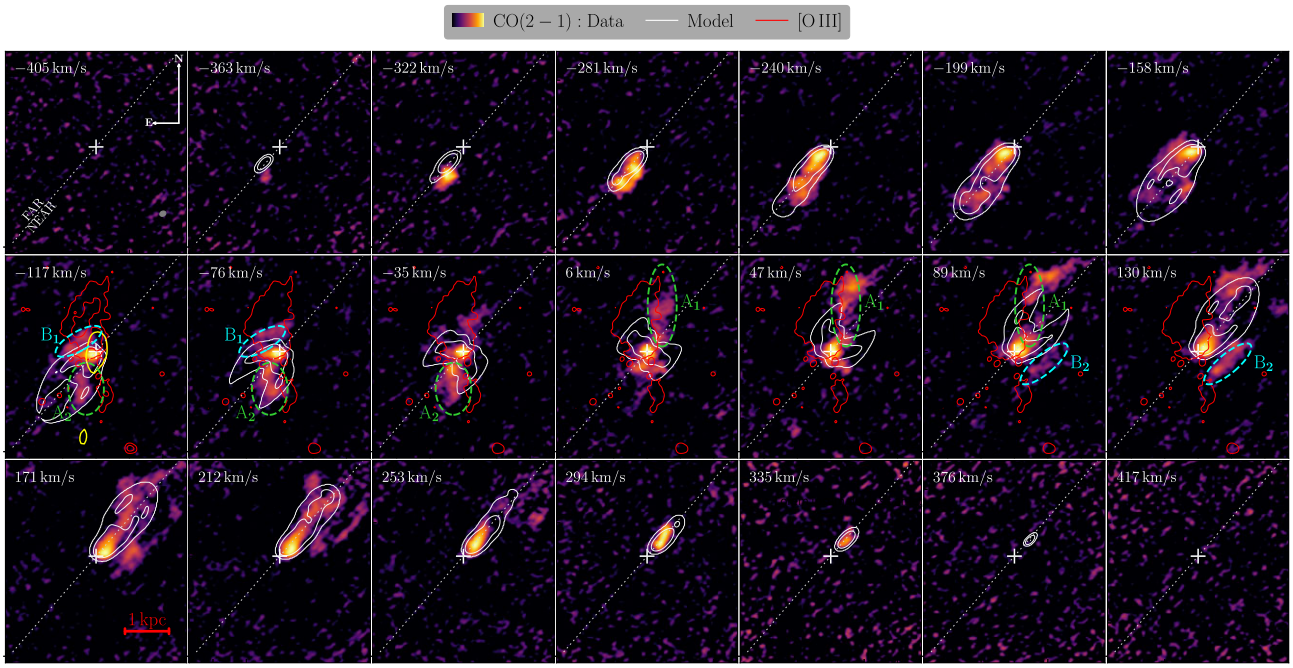

Figure 5. Channel maps of CO (2-1) from NGC 3281, with the corresponding 3D model plotted as white contours. The central velocity of the integrated channels is shown in the upper right of each panel. The green (A_1 and A_2) and blue (B_1 and B_2) dashed ovals indicate regions with discrepant kinematics between model and data, which we associated with molecular outflows and inflows, respectively (see the discussion in Section 3.2.3 and the model in Fig. 6). The [O III] ionization cone emission is shown via its outermost contour in red. In the $-117\,\mathrm{km\,s^{-1}}$ channel, we added the 8.6 GHz radio in yellow contours (see also the inset in Fig. 1)to show its projected alignment with the molecular outflow (A_2). In this channel, we also added more contours to the [O III] to emphasize its non-continuity in the B_2 region.

Fig. 5 shows that a distinct deviation appears in the channels with small absolute velocities, specially in the channels with central velocities between −117 and 89 km s^{-1}, highlighted by green dashed ellipses A_1 and A_2. In these channels, we see deviations from the rings-model along the North and South directions, where there are two 'vertical' CO emission structures that are parallel to the [O III] bipolar emission borders delineated by the red contours. On the far side of the galaxy, the CO vertical emitting structure (A_1, from channels 6 to 89 km s^{-1}) is observed running along the West side of the ionized gas [O III] emission that is above the disc. On the near side, a similar structure (A_2, between in channels −117 and −35 km s^{-1}) is also visible to the East of the [O III] emission, although less pronounced, part of the reason being that the [O III] emission is weak, since it probably originates from behind/under the galaxy disc.

The [O III] bipolar emission, which is surrounded by the CO vertical emission, has double-peaked emission line profiles with radial velocities reaching up to ∼150 km s^{-1}, which are associated with an ionized outflow (Storchi-Bergmann et al. 1992). Therefore, one possible scenario for the A_1 and A_2 features described above is that the outflow is 'multiphase', where the AGN radiation that ionizes the [O III] – and possibly drives it away from the disc in an outflow – also destroys most of the CO molecule along the bipolar region with high-excitation ionized gas. In this case, only at the borders of the bipolar/cone emission, the CO survives and is observed straddling the [O III] emission. Given that, the molecular gas in this vertical regions in the maps could also be in outflow. Since the CO (2-1) projected velocities are small in this region, the outflow itself has small velocities or its direction is close to the plane of the sky (inclination $i \sim 90°$).

This is in agreement with the model B from Storchi-Bergmann et al. (1992, see their fig. 16b, which we adapted in Fig. 6), where

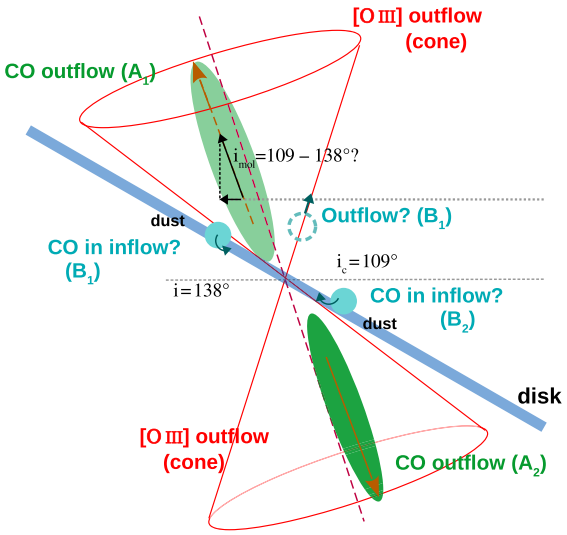

Figure 6. A scenario for the molecular gas outflow based on the Model B for the ionized gas kinematics from Storchi-Bergmann et al. (1992), under the assumption that molecular gas outflow surrounds the ionized gas one. The A_1 and A_2 green ellipses represent regions with outflowing molecular gas, which surrounds the ionized one (red cone). The B_1 and B_2 blue circles identify other CO regions with non-rotating kinematics, which are elongated, but are seen from the side in this view. Both can be interpreted as molecular inflows, located close to the disc, in dust-enhanced regions. B_2 can also be interpreted as an outflow located in the front side of the [O III] cone (dashed blue circle). These regions are also highlighted in Fig. 5.

the geometry of the bipolar [O III] outflow is a bicone with an axis with inclination $i_c = 109°$, and the border of the cone 'touches' the galaxy disc. In this case, the ionization axis makes an angle $\theta_c \sim 20°$ with the galaxy disc. Assuming that the molecular gas outflow has the same inclination $i_{mol} = i_c$ as that of the ionized gas (orange A_1 and A_2 ellipses in Fig. 6), it will reach de-projected velocities of $\sim$-360 km s^{-1} in the near side and $\sim$270 km s^{-1} in the far side. We note, however, that there is an uncertainty in the inclination of the ionization axis. In the case where i_c has a higher value, the [O III] bipolar region – depending on its opening angle – would partly intercept the disc, and the de-projected velocities would have lower values: ~ -160 km s^{-1} in the near side and $\sim$120 km s^{-1} in the far side, for the limiting case of $i_{mol} = i_d = 139°$.

There are also some CO (2-1) residuals that seem to be co-spatial – along the line of sight – with the [O III] emission. The blue dashed ellipses in the far side of the galaxy (B_1, in channels -117 and -76 km s^{-1} in Fig. 5) highlights one case: a stripe of CO emission seen $\sim$2 arcsec to the North-East of the galaxy major axis and approximately parallel to it. Following the hypothesis that the CO is destroyed by the AGN ionizing radiation, the corresponding molecular gas in this region would need to be external to the ionization cone, either behind or in front of it. In the model B from Storchi-Bergmann et al. (1992), these CO residuals (B_1) would be close to the disc, if the emission origin is behind the cone (see Fig. 6). Nevertheless, if the B_1 molecular gas were in outflow, one would expect positive velocities for this gas, but the channel maps show negative velocities. Thus, if this emission is external to the ionization cone and in outflow, it would need to be in front of the front wall of the ionization cone (dashed blue circle in the model of Fig. 6). Another possibility is that the CO emission in this B_1 region could be due to molecular gas that is in the far side of the gas disc, but not in outflow. In this case, dust could be blocking the ionizing radiation in that region, allowing the CO molecule to survive (blue circle B_1 in Fig. 6). And indeed, a close look at the [O III] emission distribution shows that it is not continuous, showing an apparent gap in this region. We have added more [O III] contour levels in the -117 km s^{-1} channel map in Fig. 5 to show this gap, but a clearer view of this discontinuity in the [O III] flux distribution can be seen in the upper-left panel of Fig. 2. This discontinuity in [O III], 'filled' with CO emission is also visible in Fig. 7 (described in the following Section 4).

There is a somewhat similar region in the near side of the galaxy disc, to the South-West – highlighted by the other blue ellipses in Fig. 5 (B_2, from channels 89 to 130 km s^{-1}). The CO emission from this region – which is also roughly parallel to the major axis – is correlated to dust lanes seen in the optical (see the darker region in the upper-left panel of Fig. 2). Therefore, the molecular gas in this region is probably in the galaxy disc (blue circle B_2 in the model of Fig. 6). The other emission seen to the North, encircled by the B_1 ellipses, could have a similar origin, since both are parallel to the major axis and separated from it by $\sim$2 arcsec, and there are also signs of a presence of dust in the B_1 region.

Given that these molecular gas B_1 and B_2 regions are not following the rotation of the galaxy disc (see Fig 3), we propose that these CO (2-1) emitting regions are close to the disc and associated to recently accreted or disturbed molecular gas (and dust). And, since B_2 is seen in redshift in the near side of the galaxy and B_1 in blueshift in the far side, these molecular clouds may be in inflow. In this case, the AGN radiation could be destroying part of the inflowing CO, ejecting it from the disc, which is what we see in the A_1 and A_2 ellipses in Fig. 5: a scenario of feeding and negative feedback – via removal of part of the molecular gas reservoir. However, given the apparent low velocities, this gas may return to the disc in the future.

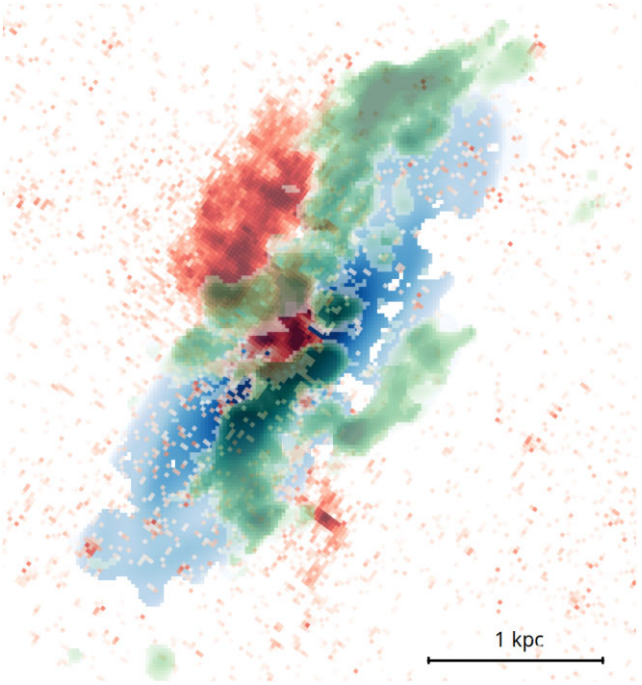

Figure 7. Superposition of the flux distribution maps of the [O III] ionized gas (red, from *HST*), the M_0 of the 3D model fitted to CO (2-1) data (blue, from the middle-right panel of Fig. C1), and the residuals from this fit (green). We only integrated the residuals from channels between -117 and 130 km s^{-1} to highlight the A_1, A_2, B_1, and B_2 regions from Fig. 5.

We note that there is also the possibility that the outflowing CO emission comes from molecular gas that cooled/condensed from the ionized gas in the cones, corresponding to '*in situ*' formation of molecular clouds (Veilleux et al. 2020). This is a proposed mechanism to account for the presence of molecular gas in winds (e.g Silich, Tenorio-Tagle & Muñoz-Tuñón 2003) and could be the origin of the gas that collapsed to form stars inside some galactic outflows, comprising the so-called 'positive feedback' (e.g. Maiolino et al. 2017; Gallagher et al. 2019).

4 DISCUSSION

In order to have a global view of the gas kinematics, we generated Fig. 7. In green, we added the flux distribution map of the CO residuals relative to rotation (from Fig. 5). We integrated between -117 and 130 km s^{-1} to include only the channels where the A_1, A_2, B_1, and B_2 are present. In blue, we superposed the the M_0 obtained from the ^{3D}BAROLO fit (middle-left panel in Fig. 3), which highlights the regions dominated by rotation. And in red, we included the [O III] ionized gas map, from the HST narrow-band image.

This figure shows that the gas that is not rotating is partially encasing the ionized gas above the galaxy plane, as well as that below the plane, suggesting a two-phase outflow, present in both the ionized and in the molecular gas. But note that not all residuals in green are necessary in outflow. Specially, the gas inside the B_1 and B_2 regions (see Fig. 5) may have other kinematics: inflows to the nuclear region, for example. The identification and analysis of the A_1, A_2, B_1, and B_2 regions were done in Section 3.2.3.

4.1 Scenario

Fig. 6 combined with Fig. 7 illustrate our proposed scenario for NGC 3281. Fig. 6 is based on one of the models proposed for the [O III] kinematics in by Storchi-Bergmann et al. (1992). Our observations and measurements, including the complex double-peaked emission line profiles, as discussed in the previous sections, reveal the presence of more than one kinematic component in the CO velocity field: part of the CO (2-1) molecular gas is in rotation in the galaxy plane, but part of it shows a contrasting kinematics, which can be interpreted as due to outflows out of the galaxy plane and also possibly inflows in the plane.

The presence of a molecular outflow, surrounding the ionized gas is supported by the flux distribution of the CO, which curves upwards and downwards from the galaxy plane: A_1 and A_2 regions in Figs 5 and 6, as well as by Fig. 7, which shows the non-rotating component of the gas kinematics surrounding the ionized gas component. The molecular gas may have been ejected from the disc, surviving the ionizing AGN radiation at the boundaries of the [O III] ionization cones.

There is also CO gas that is apparently in the galaxy plane but not following the rotating kinematics seen along the major axis (B_1 and B_2 regions in Figs 5). These regions run approximately parallel to the major axis, with the CO in the near side of the disc (region B_2) lying close to a dust lane. Given the redshift/blueshift velocities in the near/far side, the emission from these regions can be interpreted as being from molecular gas in inflow. The CO in region B_1 could also be interpreted as originating in ejected clouds in the front wall of the ionized cone, but given its similarities with B_2 region – including similar distances to the nucleus – the inflow hypothesis is more compelling.

Although the extended radio emission from NGC 3281 is weak, the southern radio blob (see Fig. 1) is located along the direction of the CO outflow A_2 region (see green contours in the $-117\,\mathrm{km\,s^{-1}}$ channel in Fig. 5). Therefore, we cannot discard that the molecular outflow seen NGC 3281 is partly driven by shocks generated by the radio-jet.

Another interesting feature is the apparent alignment between the extended [O III] and soft X-ray emission. It turns out that it is not only uncommon to find spatial correlations between the extended narrow-line region and the soft X-ray, especially in Compton-thick objects (Fabbiano & Elvis 2022) like NGC 3281 but also in other objects such as radio galaxies (Balmaverde et al. 2012). The origin of extended soft X-ray has been attribute to highly ionized emission lines (e.g. O VII, O VIII Lyα, and Ne IX), generated by AGN photoionization or shocks.

4.2 Molecular gas mass

We now use the CO emission inside the A_1 and A_2 regions (green ellipses in Fig. 5) to calculate the total outflowing molecular gas mass. The total flux in emission was integrated inside a 10 arcsec ($\sim$2.3 kpc) radius to avoid adding the contribution from the CO emission observed beyond this radius, which may be artefacts of the data reduction (see lower panels of Fig. 2). Including it would increase that total mass by $\sim$6 per cent.

The total flux emitted inside these outflowing regions is $(S_\nu \Delta \mathrm{v})_{\mathrm{out}} \sim 1.6\,\mathrm{Jy\,km\,s^{-1}}$, which translates to a CO (2-1) luminosity of $L'_{\mathrm{CO\,(2-1),out}} \sim 2.3 \times 10^6\,\mathrm{K\,km\,s^{-1}\,pc^{-2}}$ (Solomon et al. 1997). Following Ramos Almeida et al. (2022), for a conversion factor of $\alpha_{CO} = 0.8 \pm 0.5\,\mathrm{M_\odot (K\,km\,s^{-1}\,pc^{-2})^{-1}}$ (Morganti et al. 2015) and a ratio $L'_{\mathrm{CO\,(2-1)}}/L'_{\mathrm{CO\,(1-0)}} = 1$ (Braine & Combes 1992; Carilli & Walter 2013), we obtain a total molecular mass in outflow of $M_{\mathrm{mol,\,out}} = (2.5 \pm 1.6) \times 10^6\,\mathrm{M_\odot}$, which is distributed equally between regions A_1 and A_2. As a comparison, the total molecular gas mass in emission is $M_{\mathrm{mol,EM}} = (1.5 \pm 0.9) \times 10^8\,\mathrm{M_\odot}$ ($S_\nu \Delta \mathrm{v} \sim 95.3\,\mathrm{Jy\,km\,s^{-1}}$). Therefore, the corresponding fraction is $M_{\mathrm{mol,out}}/M_{\mathrm{mol,EM}} \sim 1.7$ per cent, where we are assuming the same α_{CO} value for the $M_{\mathrm{mol,\,out}}$ and $M_{\mathrm{mol,EM}}$. If we assumed that gas inside the B_1 region was also outflowing, this fraction would be $\sim$2 per cent. The molecular mass values were multiplied by a factor of 1.36 to account for the presence of He and heavier elements (Saintonge & Catinella 2022).

Using the compilation made by Ramos Almeida et al. (2022), we note that the NGC 3281 fraction of molecular gas mass in outflow is higher than the values found by the authors for their QSOs (in the range 0.1–1 per cent; Ramos Almeida et al. 2022) and for other Seyfert galaxies (0.2–0.7 per cent; Alonso-Herrero et al. 2019; Domínguez-Fernández et al. 2020; García-Bernete et al. 2021). Aside from that, the $M_{\mathrm{mol,out}}/M_{\mathrm{mol,EM}}$ values from NGC 3281 are similar to those found in jetted Seyferts (3–5 per cent; García-Burillo et al. 2014; Morganti et al. 2015) and ULIRG AGNs (2–27 per cent; Feruglio et al. 2010; Cicone et al. 2014).

4.3 Molecular mass outflow rate and power

To evaluate the strength of the molecular outflow, we measured the mass outflow rate ($\dot{M}_{\mathrm{out,mol}}$) and outflow power ($\dot{E}_{\mathrm{out,mol}}$). The contribution from each velocity channel was calculated separately, and resulting values integrated. We applied two methods over the regions delimited by the A_1 and A_2 ellipses in Fig. 5, using channels with the projected velocities (6, 47, and 89) $\mathrm{km\,s^{-1}}$ and (-117, -76, and -35) $\mathrm{km\,s^{-1}}$, respectively.

4.3.1 Method 1: average

The first method assumes that the rates do not vary along the radii, with the resulting values corresponding to averages of these quantities. For this, we consider a fixed outflow radius $R_{\mathrm{out}}(\mathrm{v}_i)$ for each channel, with the respective outflow mass $M_{\mathrm{mol,\,out}}(\mathrm{v}_i)$ being integrated inside each of the elliptical regions. Only spaxels with flux density above σ_{RMS} are considered. The corresponding formulas are:

$$\dot{M}_{\mathrm{out,mol}} = \sum_{\mathrm{v}_i} \frac{\mathrm{v}_i \cdot M_{\mathrm{mol,out}}(\mathrm{v}_i)}{R_{\mathrm{out}}(\mathrm{v}_i)} \quad (1)$$

$$\dot{E}_{\mathrm{out,mol}} = \sum_{\mathrm{v}_i} \frac{1}{2} \cdot \mathrm{v}_i^2 \dot{M}_{\mathrm{mol,out}}(\mathrm{v}_i). \quad (2)$$

In order to avoid overestimation of the sizes due to spurious spaxels, we first convolved the map of each channel by a beam-shape 2D Gaussian. We then measured the distance along each ellipse from the closest to farthest spaxel with flux density above σ_{RMS}. The measured projected distances ($R_{\mathrm{out}}(\mathrm{v}_i)$) obtained for the channels of the A_1 region were (6.3, 6.75, and 6.9 arcsec), and (4.5, 4.4, and 4.3 arcsec) for the A_2 region.

To correct for projection effects, we considered two inclinations i_{mol} for the molecular outflow: one equal to the inclination of ionization axis $i_c = 109^\circ$ (from Storchi-Bergmann et al. 1992) and another equal to the inclination of the disc $i_d = 139^\circ$, for the case of the molecular outflow axis being closer to the disc. We corrected the projected velocities ($\mathrm{v_{proj}}$) and radii/sizes (r_{proj}) using: $\mathrm{v} = \mathrm{v_{proj}}/|\cos(i_{\mathrm{mol}})|$ and $r = r_{\mathrm{proj}}/\sin(i_{\mathrm{mol}})$.

For an inclination of $i_{\mathrm{mol}} = 139^\circ$, we obtained values of $\dot{M}^{\mathrm{avg}}_{\mathrm{out,mol}} = 0.12 \pm 0.04\,\mathrm{M_\odot\,yr^{-1}}$ and $\dot{E}^{\mathrm{avg}}_{\mathrm{out,mol}} = (4.8 \pm$

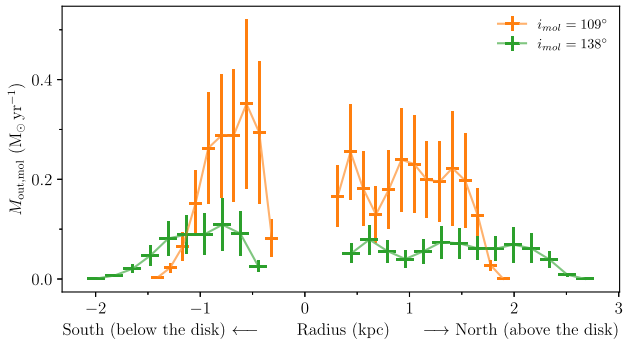

Figure 8. Radial profiles of the molecular mass outflow rate $M_{\rm out,\,mol}$ from the nucleus of NGC 3281 as a function of the de-projected radius. $M_{\rm out,\,mol}$ values in orange and green correspond to outflow inclinations $i_{\rm mol}$ of 109° and 139°, respectively.

$1.7) \times 10^{38}$ erg s^{-1}. And for an inclination of $i_{\rm mol} = 109°$, we obtained values of $\dot{M}^{\rm avg}_{\rm out,mol} = 0.39 \pm 0.12\,{\rm M}_\odot\,{\rm yr}^{-1}$ and $\dot{E}^{\rm avg}_{\rm out,mol} = (8.1 \pm 2.9) \times 10^{39}$ erg s^{-1}. Therefore, depending on the inclination, the values of $\dot{M}_{\rm out,mol}$ and $\dot{E}_{\rm out,mol}$ differ by a factor of ∼3 and ∼17, respectively, with the factors being equal for the following method 2. The uncertainty are the result of propagating the uncertainty from α_{CO}.

4.3.2 Method 2: radial profiles

The second method, is based in generating the radial of profiles of $\dot{M}_{\rm out,mol}(r)$ and $\dot{E}_{\rm out,mol}(r)$, as shown in Fig. 8 for the first quantity. For each ring at radius r, with a defined thickness $\delta r = {\rm FWHM_{mean}} = 0.5$ arcsec, we calculate:

$$\dot{M}_{\rm out,mol}(r) = \sum_{\rm v_i} \frac{{\rm v}_i \cdot M_{\rm mol,out}({\rm v}_i)}{\delta r}, \quad (3)$$

and analogous for $\dot{E}_{\rm out,mol}(r)$. In this case, we integrated the contribution from channels inside A_1 (North, above the disc) and A_2 (South, below the disc), separately.

Above the disc (North), where the CO (2-1) emission is less absorbed by the gas/dust in the disc, the $\dot{M}_{\rm out,mol}(r)$ is somewhat constant up to a radius of ∼1.5–2.2 kpc (depending on the inclination $i_{\rm mol}$). Below the disc, it reaches a peak value at ∼0.5–0.8 kpc, and is approximately constant up to ∼0.9–1.3 kpc. The maximum outflow extent is $R^{\rm max}_{\rm out} \sim 7.5$ arcsec ∼ 1.8–2.6 kpc.

To compare our data with results from the literature and the method 1 above (see Section 4.3.1), we measured the peak values of $\dot{M}_{\rm out,mol}$ and $\dot{E}_{\rm out,mol}$ (e.g Dall'Agnol de Oliveira et al. 2021; Trindade Falcão et al. 2021). For this, we added the contribution from each side of the cone (north and south), such that the following resulting values correspond to the maximum rates of mass crossing rings/spheres with a fixed δr. We obtained maximum values of $\dot{M}^{\rm max}_{\rm out,mol} = 0.55 \pm 0.17{\rm M}_\odot\,{\rm yr}^{-1}$ and $\dot{E}^{\rm max}_{\rm out,mol} = 1.2 \pm 0.5 \times 10^{40}$ erg s^{-1} for $i_{\rm mol} = 109°$, at a radius of 0.4–0.6 kpc.

Considering mass outflow rates obtained from both inclinations, the maximum range obtained from the method 2 (peak of the radial profiles) is $\dot{M}^{\rm max}_{\rm out,mol} = 0.12$–$0.72\,{\rm M}_\odot\,{\rm yr}^{-1}$, which is in agreement with the results from the method 1 (the average values) $\dot{M}^{\rm avg}_{\rm out,mol} = 0.08$–$0.5\,{\rm M}_\odot\,{\rm yr}^{-1}$. The same is true for molecular outflow power, with ranges of $\dot{E}^{\rm max}_{\rm out,mol} = (0.045$–$1.6) \times 10^{40}$ erg s^{-1} and $\dot{E}^{\rm avg}_{\rm out,mol} = (0.031$–$1.1) \times 10^{40}$ erg s^{-1}. Therefore, we chose to use $\dot{M}^{\rm max}_{\rm out,mol}$ and $\dot{E}^{\rm max}_{\rm out,mol}$ as the default values in the remaining of the paper. From the compilation made by Ramos Almeida et al. (2022), the mass outflow rate of NGC 3281 falls at the low end of other Seyferts (∼0.3–5 ${\rm M}_\odot\,{\rm yr}^{-1}$), with more energetic sources like QSOs and ULIRGs having higher values of $\dot{M}_{\rm out,mol}$, by up to ∼3 orders of magnitude.

To include the contribution from the ionized gas, we calculate the ionized outflow power from the data collected from Storchi-Bergmann et al. (1992). We used a total ionized gas mass (from Hβ) of $M_{\rm ion} \sim 2 \times 10^6\,{\rm M}_\odot$, a [O III] de-projected ouflow radial velocity and velocity dispersion of ${\rm v_{out,ion}} \sim 150\,{\rm km\,s^{-1}}$ and $\sigma_{\rm out,ion} \sim 150\,{\rm km\,s^{-1}}$, and a de-projected ionized outflow extent of $R_{\rm out,ion} \sim 2$ kpc. Since the available data are not separated by channels (as the molecular data from our work), we calculated the outflow power using: $\dot{E}_{\rm out} = 0.5 \cdot ({\rm v}^2 + \sigma^2) \cdot {\rm v} \cdot \dot{M}/R$, for the conservative case of B = 1 (Harrison et al. 2018). The resulting ionized outflow power is $\dot{E}_{\rm out,ion} \sim 10^{39}$ erg s^{-1}. Therefore, considering the uncertainties, we cannot distinguish if the outflow power is stronger in the molecular or the ionized phase.

4.3.3 Coupling efficiency

To gauge the impact that the molecular outflow may have on the evolution of NGC 3281, we calculated the per cent of AGN luminosity ($L_{\rm AGN}$) that couples kinetically with the molecular gas via outflows: the kinetic coupling efficiency $\varepsilon_{f,\rm mol} = \dot{E}_{\rm out,mol}/L_{\rm AGN}$. For this, we used a luminosity of $L_{\rm Bol} = 10^{44.3\,\pm\,0.4}$ erg s^{-1} (see Section 1), and since the method 1 and 2 returned similar values (Sections 4.3.1 and 4.3.2), we used the peak value from the radial profile $\dot{E}_{\rm out,mol}$ as the kinetic power.

Therefore, the resulting $\varepsilon_{f,\rm mol}$ of the outflowing molecular gas ranges between 10^{-4} and 0.02 per cent. This value is, at least, 1 order of magnitude lower than the ∼0.5 per cent value required in models (e.g. Hopkins & Elvis 2010; Zubovas 2018) to produce a significant impact in the galaxy and influence its evolution. Adding the contribution from $\dot{E}_{\rm out,ion}$ and assuming that only 20 per cent of energy couples kinematically with the gas (Richings & Faucher-Giguère 2018), the maximum value ε_f is still only 0.1 per cent.

Hence, given the current energy involved in the AGN feedback of NGC 3281, we do not expect that the evolution of host galaxy to be affected globally over a short period of time. But we note that, since the molecular gas is being expelled from the inner regions, the star formation in the nuclei will be at least partially affected in a short period of time. This is in agreement with the results found by Storchi-Bergmann et al. (1992) from the equivalent width of optical stellar absorption lines. The values indicate a dominant old stellar population within 2.3 kpc of the nucleus, typical of the bulges of early-type galaxies, even though NGC 3281 morphology is dominated by the disc, with a bulge-to-total flux of B/T ∼ 0.1 (Gao et al. 2019). In contrast, Stone et al. (2016) obtained an SFR of $\sim 7\,{\rm M}_\odot\,{\rm yr}^{-1}$ in NGC 3281, from the luminosity at 160 μm. This value would put NGC 3281 above the star formation main sequence (e.g. Elbaz et al. 2007), given its total stellar mass of $10^{8.6}$–$10^{10.24}\,{\rm M}_\odot$ (see Section 1). Considering only the molecular gas outflow, the corresponding mass-loading factor $\eta_{\rm mol} = \dot{M}_{\rm out,mol}/{\rm SFR} \sim 0.02$–$0.1$ reinforces the conclusion that the AGN feedback in NGC 3281 is not strongly regulating the star formation, given that galaxy evolution models usually require $\eta \sim 1$ (Veilleux et al. 2020).

4.4 Comparison with previous studies

A similar molecular gas outflow – surrounding an ionized outflow – has been observed in CO (1-0) in the starburst galaxy NGC 253 (Bolatto et al. 2013b), where the corresponding $\dot{M}_{\rm out,mol}$ is 3–9 ${\rm M}_\odot\,{\rm yr}^{-1}$,

an order-of-magnitude higher than our value for NGC 3281. This galaxy has a total stellar mass of $M_* \sim 10^{10.5}$ M$_\odot$ (Bailin et al. 2011; Lucero et al. 2015), while NGC 3281 apparently has a lower stellar mass, with a value ranging between $10^{8.6}$ and $10^{10.24}$ M$_\odot$ (see Section 1). Therefore, the difference in the host M_* may affect a direct comparison between the two galaxies, with the same being true for the other galaxies discussed below.

In our own galaxy, the Milk Way [$M_* \sim 10^{10.8}$ M$_\odot$, from McMillan (2011)], the molecular line CS (2-1) emission map displays an 'hourglass' morphology (Hsieh et al. 2016), surrounding the base of a cavity – filled with X-ray/radio lobes (similar to our Fig. 1) (Bland-Hawthorn & Cohen 2003; Heywood et al. 2019; Ponti et al. 2019) – that may have been caused by a previous outflow (Veilleux et al. 2020). The scales involved, however, are much smaller in the Milky Way, which has an outflow extent of only ∼13 pc and maximum velocities of ∼100 km s^{-1}.

Going to higher stellar masses, in the central galaxy of the Phoenix cluster (Phoenix A, with M_* estimated by McDonald et al. (2014) to be $\sim 10^{11.9}$ M$_\odot$), the CO (3-2) intensity map displays a similar pattern to that observed in our M_0 map (Figs 1 and 2). Both present an S-shape morphology, and, in the case of Phoenix A, the CO surrounds the edges of a bipolar X-ray emission (Russell et al. 2017). However, in the case of the Phoenix galaxy, the [O III] seems to extend along the CO emission (McDonald et al. 2014), and a radio jet-driven bubble is argued to be responsible for the X-ray cavities and to drive the molecular gas outflow encasing these cavities (Russell et al. 2017). Other examples of the molecular gas avoiding/surrounding radio lobes include the young radio galaxy PKS 0023–26 (Morganti et al. 2021) and the 3C 305 (Morganti et al. 2023).

Other Seyfert galaxies present similar features in the hot molecular gas, measured via H_2 lines in the near-infrared. The hot H_2 has been detected in regions surrounding the ionization axis, sometimes even showing an 'hourglass' shape, in objects like NGC 4151 (May et al. 2020), MRK 573 (Fischer et al. 2017), and NGC 1068 (May & Steiner 2017), with the latter also showing a similar distribution in CO (3-2) (García-Burillo et al. 2016). All these objects also present radio jets along the ionization axis, and most of them show signs of hot molecular gas outflows.

5 CONCLUSIONS

We analysed the cold molecular gas distribution and kinematics of the Seyfert 2 galaxy NGC 3281 using observations of the CO (2-1) line. For such, we employed ALMA observations with an angular resolution of 0.5 arcsec (∼100 pc). The main results are:

(i) We found an anticorrelation between the spatial distribution of the CO molecular gas emission – mostly seen in the galaxy plane – and that of the ionized gas, which shows a biconical geometry previously observed in the optical [O III]. The total molecular gas mass seen in emission is $M_{\rm mol,EM} = (1.5 \pm 0.9) \times 10^8$ M$_\odot$.

(ii) Although most CO emission comes from the galaxy plane, we found it also surrounding the bipolar cones. This is supported by the M_0 moment, which shows CO emission extending upwards and downwards from the plane. Its distribution suggests that part of the molecular gas is leaving the galaxy plane in the nuclear region but is being destroyed along the AGN ionization axis.

(iii) The CO kinematics is dominated by rotation in the galaxy plane, as shown by the fit of a 3D model to the CO (2-1) data cube. The mean inclination of the disc and position angle of its axis were found to be $i_d = 139°$ and PA = 73°, with the systemic velocity corresponding to a redshift of z = 0.01124.

(iv) From the residuals between the data and the rotation model, we identified two regions where the CO is tracing molecular gas outflows. One above the disc, and another below, both at the edges of the [O III] cones. Depending on the assumed molecular outflow inclination ($i_{mol} = 139°$ or 109°), it reaches maximum velocities of 160–360 km s^{-1}, extending up to $R_{\rm out}^{\rm max} \sim 1.8$–2.6 kpc from the nucleus.

(v) The corresponding molecular mass in outflow is $M_{\rm mol,\,out} = (2.5 \pm 1.6) \times 10^6$ M$_\odot$ and represents ∼1.7 per cent of the total emitting molecular gas mass emission $M_{\rm mol,EM}$. If we assume that the gas inside the B_1 regions are also outflowing, this fraction becomes $M_{\rm mol,out}/M_{\rm mol,EM} \sim 2$ per cent,.

(vi) The mass outflow rate is $\dot{M}_{\rm out,mol} = 0.12$–$0.72$ M$_\odot$ yr^{-1} (depending on $i_{\rm mol}$). These values correspond to the peak of the radial profiles of $\dot{M}_{\rm out,mol}(r)$. The corresponding molecular outflow power is $\dot{E}_{\rm out,mol} = (0.045$–$1.6) \times 10^{40}$ erg s^{-1}, which translates to a molecular kinetic efficiency of 10^{-4}–0.02 per cent. Including the contribution of the ionized outflow and assuming that only 20 per cent of the AGN feedback couples kinetically with the gas, the maximum value of the coupling efficiency of the AGN feedback with the surroundings only reaches ∼0.1 per cent.

(vii) There are other two regions with distinct CO residuals that do not follow a rotation pattern, in patches running parallel to the major axis. Both can be interpreted as molecular inflow in the disc, given the corresponding velocities and the correlation with dust. One of them, however, could also be interpreted as being in outflow in front of the [O III] cone. None the less, the interpretation of molecular gas in these regions is uncertain, and we do not attempt to calculate the corresponding rates of inflow/outflow.

The CO outflow geometry in NGC 3281 – encasing the ionized gas, is similar to those seen in other sources like NGC 256, Milky Way, and Perseus A, where the molecular gas outflow surrounds the ionized gas cone and/or the X-ray/radio emission. These results suggest that such molecular outflows can be common in active galaxies. But they can only be found with a careful analysis of the molecular gas distribution and kinematics to separate gas rotating in the galaxy plane from that in outflow.

We also note that the low coupling efficiency and small/medium velocities indicate that the current feedback probably will not affect much the evolution of the host galaxy NGC 3281, at least over larger scales. However, the expelling of molecular gas from inner regions will diminish the SFR over short periods of time, since it ends up removing a fraction of the fuel available to form new stars.

ACKNOWLEDGEMENTS

This paper makes use of the following ALMA data: ADS/JAO.ALMA#2018.1.00211.S. ALMA is a partnership of ESO (representing its member states), NSF (USA), and NINS (Japan), together with NRC (Canada), MOST and ASIAA (Taiwan), and KASI (Republic of Korea), in cooperation with the Republic of Chile. The Joint ALMA Observatory is operated by ESO, AUI/NRAO, and NAOJ.

This study was financed in part by the Coordenação de Aperfeiçoamento de Pessoal de Nível Superior (CAPES-Brasil, 88887.478902/2020-00). RAR acknowledges the support from Conselho Nacional de Desenvolvimento Científico e Tecnológico (CNPq) and Fundação de Amparo à pesquisa do Estado do Rio Grande do Sul (FAPERGS).

This work made use of ASTROPY: a community-developed core PYTHON package and an ecosystem of tools and resources for astron-

omy (Astropy Collaboration 2013). We also used the SPECTRALCUBE package (Ginsburg et al. 2019) to manipulate the data cube and MATPLOTLIB (Hunter 2007) to generate the figures.

DATA AVAILABILITY

The data used in this paper are publicly available at the ALMA Science Archive under the program code 2018.1.00211.S. Processed data can be shared on reasonable request to the corresponding author.

REFERENCES

Alonso-Herrero A. et al., 2019, A&A, 628, A65
Alves J., Lada C. J., Lada E. A., 1999, ApJ, 515, 265
Asmus D., Hönig S. F., Gandhi P., Smette A., Duschl W. J., 2014, MNRAS, 439, 1648
Astropy Collaboration, 2013, A&A, 558, A33
Bailin J., Bell E. F., Chappell S. N., Radburn-Smith D. J., de Jong R. S., 2011, ApJ, 736, 24
Balmaverde B. et al., 2012, A&A, 545, A143
Begeman K. G., 1987, PhD thesis, University of Groningen, Kapteyn Astronomical Institute
Bischetti M., Maiolino R., Carniani S., Fiore F., Piconcelli E., Fluetsch A., 2019, A&A, 630, A59
Bland-Hawthorn J., Cohen M., 2003, ApJ, 582, 246
Bolatto A. D., Wolfire M., Leroy A. K., 2013a, ARA&A, 51, 207
Bolatto A. D. et al., 2013b, Nature, 499, 450
Braine J., Combes F., 1992, A&A, 264, 433
Cano-Díaz M., Maiolino R., Marconi A., Netzer H., Shemmer O., Cresci G., 2012, A&A, 537, L8
Carilli C. L., Walter F., 2013, ARA&A, 51, 105
Cavagnolo K. W., McNamara B. R., Nulsen P. E. J., Carilli C. L., Jones C., Bîrzan L., 2010, ApJ, 720, 1066
Cicone C. et al., 2014, A&A, 562, A21
Cicone C., Brusa M., Ramos Almeida C., Cresci G., Husemann B., Mainieri V., 2018, Nature Astron., 2, 176
Circosta C. et al., 2021, A&A, 646, A96
Dall'Agnol de Oliveira B. et al., 2021, MNRAS, 504, 3890
Di Matteo T., Springel V., Hernquist L., 2005, Nature, 433, 604
Di Teodoro E. M., Fraternali F., 2015, MNRAS, 451, 3021
Domínguez-Fernández A. J. et al., 2020, A&A, 643, A127
Elbaz D. et al., 2007, A&A, 468, 33
Fabbiano G., Elvis M., 2022, The Interaction of the Active Nucleus with the Host Galaxy Interstellar Medium, Handbook of X-ray and Gamma-ray Astrophysics, Springer Nature Singapore, Singapore
Fabian A. C., 2012, ARA&A, 50, 455
Feruglio C., Maiolino R., Piconcelli E., Menci N., Aussel H., Lamastra A., Fiore F., 2010, A&A, 518, L155
Fischer T. C. et al., 2017, ApJ, 834, 30
Gallagher R., Maiolino R., Belfiore F., Drory N., Riffel R., Riffel R. A., 2019, MNRAS, 485, 3409
Gao H., Ho L. C., Barth A. J., Li Z.-Y., 2019, ApJS, 244, 34
García-Bernete I. et al., 2021, A&A, 645, A21
García-Burillo S. et al., 2014, A&A, 567, A125
García-Burillo S. et al., 2016, ApJ, 823, L12
Ginsburg A. et al., 2019, radio-astro-tools/spectral-cube: Release v0.4.5, Zenodo,
Harrison C. M., Costa T., Tadhunter C. N., Flütsch A., Kakkad D., Perna M., Vietri G., 2018, Nature Astronomy, 2, 198
Haynes M. P. et al., 2011, AJ, 142, 170
Heckman T. M., Best P. N., 2014, ARA&A, 52, 589
Heckman T. M., Kauffmann G., Brinchmann J., Charlot S., Tremonti C., White S. D. M., 2004, ApJ, 613, 109
Hess K. M., Jarrett T. H., Carignan C., Passmoor S. S., Goedhart S., 2015, MNRAS, 452, 1617
Heywood I. et al., 2019, Nature, 573, 235
Ho L. C., Li Z.-Y., Barth A. J., Seigar M. S., Peng C. Y., 2011, ApJS, 197, 21
Hopkins P. F., Elvis M., 2010, MNRAS, 401, 7
Hsieh P.-Y., Ho P. T. P., Hwang C.-Y., Shimajiri Y., Matsushita S., Koch P. M., Iono D., 2016, ApJ, 831, 72
Hunter J. D., 2007, Comput. Sci. Eng., 9, 90
Husemann B., Scharwächter J., Bennert V. N., Mainieri V., Woo J. H., Kakkad D., 2016, A&A, 594, A44
Jarvis M. E. et al., 2019, MNRAS, 485, 2710
Jarvis M. E. et al., 2020, MNRAS, 498, 1560
Ji Z., Giavalisco M., Kirkpatrick A., Kocevski D., Daddi E., Delvecchio I., Hatcher C., 2022, ApJ, 925, 74
Kim C. et al., 2022, ApJ, 928, 73
Koss M., Mushotzky R., Veilleux S., Winter L. M., Baumgartner W., Tueller J., Gehrels N., Valencic L., 2011, ApJ, 739, 57
Lucero D. M., Carignan C., Elson E. C., Randriamampandry T. H., Jarrett T. H., Oosterloo T. A., Heald G. H., 2015, MNRAS, 450, 3935
Ma J., Elvis M., Fabbiano G., Baloković M., Maksym W. P., Jones M. L., Risaliti G., 2020, ApJ, 900, 164
Maiolino R. et al., 2017, Nature, 544, 202
May D., Steiner J. E., 2017, MNRAS, 469, 994
May D., Steiner J. E., Menezes R. B., Williams D. R. A., Wang J., 2020, MNRAS, 496, 1488
McDonald M. et al., 2014, ApJ, 784, 18
McMillan P. J., 2011, MNRAS, 414, 2446
Morganti R., 2017, Front. Astron. Space Sci., 4, 42
Morganti R., Tsvetanov Z. I., Gallimore J., Allen M. G., 1999, A&AS, 137, 457
Morganti R., Oosterloo T., Oonk J. B. R., Frieswijk W., Tadhunter C., 2015, A&A, 580, A1
Morganti R., Oosterloo T., Tadhunter C., Bernhard E. P., Raymond Oonk J. B., 2021, A&A, 656, A55
Morganti R., Murthy S., Guillard P., Oosterloo T., Garcia-Burillo S., 2023, Galaxies, 11, 24
Naab T., Ostriker J. P., 2017, ARA&A, 55, 59
Nelson D. et al., 2019, MNRAS, 490, 3234
Oh K. et al., 2018, ApJS, 235, 4
Ponti G. et al., 2019, Nature, 567, 347
Ramakrishnan V. et al., 2019, MNRAS, 487, 444
Ramos Almeida C. et al., 2022, A&A, 658, A155
Richings A. J., Faucher-Giguère C.-A., 2018, MNRAS, 478, 3100
Rosario D. J. et al., 2018, MNRAS, 473, 5658
Rubin V. C., Burstein D., Ford W. K. J., Thonnard N., 1985, ApJ, 289, 81
Russell H. R. et al., 2017, ApJ, 836, 130
Saintonge A., Catinella B., 2022, ARA&A, 60, 319
Sales D. A., Pastoriza M. G., Riffel R., Winge C., Rodríguez-Ardila A., Carciofi A. C., 2011, ApJ, 738, 109
Salvestrini F. et al., 2022, A&A, 663, A28
Schaye J. et al., 2015, MNRAS, 446, 521
Schmitt H. R., Donley J. L., Antonucci R. R. J., Hutchings J. B., Kinney A. L., 2003, ApJS, 148, 327
Silich S., Tenorio-Tagle G., Muñoz-Tuñón C., 2003, ApJ, 590, 791
Silk J., Mamon G. A., 2012, Res. Astron. Astrophys., 12, 917
Solomon P. M., Downes D., Radford S. J. E., Barrett J. W., 1997, ApJ, 478, 144
Spence R. A. W., Tadhunter C. N., Rose M., Rodríguez Zaurín J., 2018, MNRAS, 478, 2438
Stone M., Veilleux S., Meléndez M., Sturm E., Graciá-Carpio J., González-Alfonso E., 2016, ApJ, 826, 111
Storchi-Bergmann T., Wilson A. S., Baldwin J. A., 1992, ApJ, 396, 45
Trindade Falcão A. et al., 2021, MNRAS, 500, 1491
Vasudevan R. V., Fabian A. C., Gandhi P., Winter L. M., Mushotzky R. F., 2010, MNRAS, 402, 1081
Veilleux S., Maiolino R., Bolatto A. D., Aalto S., 2020, A&AR, 28, 2
Vignali C., Comastri A., 2002, A&A, 381, 834
Ward S. R., Harrison C., Costa T., Mainieri V., 2022, MNRAS, 514, 2936
Winter L. M., Mushotzky R. F., Reynolds C. S., Tueller J., 2009, ApJ, 690, 1322
Zubovas K., 2018, MNRAS, 479, 3189

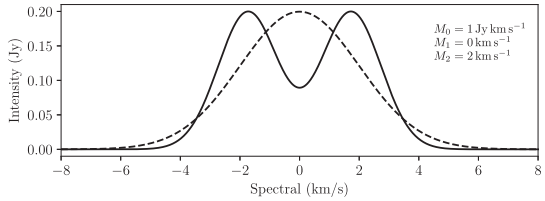

Figure A1. Two (synthetic) distinct emission-line profiles that have the same M_0, M_1, and M_2 moments values.

APPENDIX A: MOMENTS

For each spaxel, the moments were calculated as:

$$M_0 = \sum S(\mathrm{v})\Delta\mathrm{v} \tag{A1}$$

$$M_1 = \frac{\sum \mathrm{v}\, S(\mathrm{v})\Delta\mathrm{v}}{M_0} \tag{A2}$$

$$M_2 = \sqrt{\frac{\sum(\mathrm{v} - M_1)^2 S(\mathrm{v})\Delta\mathrm{v}}{M_0}}, \tag{A3}$$

where M_0 is the total flux of the line profile, while M_1 and M_2 are the intensity-weighted radial velocity and velocity dispersion (a measure of the internal disturbance of the gas), respectively. The flux density ($S(\mathrm{v})$) are in units of Jy beam^{-1}, while the channel central velocity (v) and width (Δv) are in km s^{-1}. For a perfect Gaussian profile, $M_1 = v$ (the radial velocity) and $M_2 = \sigma$ (velocity dispersion). But we note that, in some cases, the moments can hide more complex profiles. An example is shown in Fig. A1, where one simple Gaussian and a double-peaked profile – possibly denoting the presence of two kinematic components – the same values for their moments M_0, M_1, and M_2.

APPENDIX B: MASKS

To explain how the mask used to identify regions with dominating CO emission lines was created, in Fig. B1, we show how the M_1 map is affected when different masks are used.

First, we selected all spaxels that have at least one spectral value above $3\,\sigma_{\mathrm{RMS}}$, generating a 2D mask from remaining ones (left-hand panel of Fig. B1). Using only this criterion, a lot of spurious spaxels are not masked.

To "clean" these isolated spaxels, we smoothed the mask spatially with a 2D Gaussian with $\sigma = 1$ pix. This was done to the mask in a binary (0 and 1 values) form. Then, any spaxels with resulting values lower than 0.5 were and masked. This process masks isolated group with less then 5 spaxels (area ∼8 times smaller then the beam one) and was repeated until a convergence was achieved. The middle panel shows the M_1 obtained with the resulting mask.

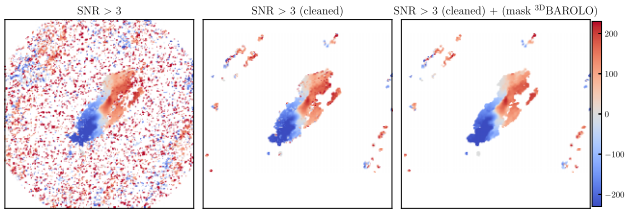

Figure B1. M_1 map calculated using different masks. Left: all spaxels whose spectra do not have flux density values above $3\,\sigma_{\mathrm{RMS}}$ are masked. Centre: the left 2D mask after being cleaned,.
by using a cutting threshold applied to a smoothed version of the mask. Right: The combination of the mask from the middle with the 3D mask produced by 3DBAROLO, which uses a similar threshold method applied to the cube (channel by channel).

However, since this is a 2D mask, spurious values along the spectral dimension can still affect the final moment values. Therefore, we combine the 2D mask with the 3D one produced by 3DBAROLO using the "SMOOTH" option – with the default parameters SCALEFACTOR = 2 and BLANKCUT = 3 – that smooths each channel of the cube individually and masks them based on the resulting signal-to-noise ratio. The resulting 3D mask was combined with the 2D one and used to obtain the final moment maps (see right-hand panel of Figs B1, 2, and 3).

APPENDIX C: ADDITIONAL FIGURES

Fig. C1 shows the results of the fit of a 2D model (Begeman 1987) on the first moment of CO (2-1) (M_1).

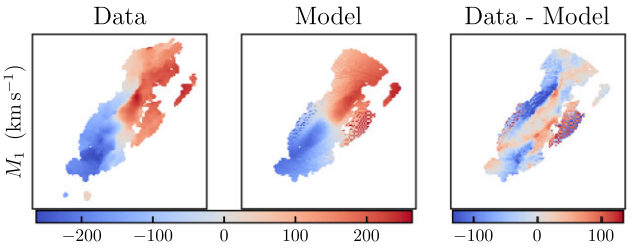

Figure C1. Fitting results of the 2D model (Begeman 1987) fitted to M_1 kinematics using 3DBAROLO. The first, second, and third columns correspond to M_1 data, the 2D model, and the corresponding residuals, respectively.

This paper has been typeset from a TEX/LATEX file prepared by the author.